Host-Derived Localized Acidification Triggers Chaperone-Primed Effector Unfolding at the T3SS Gate

Qiong Xing

qiongxingnmr@hubu.edu.cn

Hubei University https://orcid.org/0000-0003-0213-8364

Wenxue Jiang

Hubei University

Miao Wu

Hubei University

Xiaoqi Cheng

Hubei University

Dujuan Shi

Hubei University

Xu Dong

Hubei University

Zhou Gong

Chinese academy of Science

Lixin Ma

Hubei University https://orcid.org/0000-0002-2016-9781

Article

Keywords: Host-contact triggering, Localized acidification/T3SS regulation, Chapreone priming, Effector unfolding, Processive translocation

Posted Date: June 2nd, 2026

DOI: https://doi.org/10.21203/rs.3.rs-9571766/v1

Additional Declarations: There is **NO** Competing Interest.

Abstract

Pathogenic bacteria using type secretion system (T3SS) to inject effectors into host cells through a narrow channel, requiring complete substrate unfolding at the point of secretion. However, the regulatory logic integrating host-derived cues to license this decisive conformational switch has remained enigmatic. Here, we discover that host-cell attachment generates a localized acidic microenvironment (pH ~ 5.6) at the cytoplasmic face of the T3SS export apparatus, which directly triggers the unfolding of chaperone-primed effectors. We demonstrate that T3SS chaperones function as active conformational primers, dismantling effector stability to create a metastable, pH-sensitive state. Protonation of histidine-based sensors catalyzes primed effectors unfolding, enabling selective recognition by the gatekeeper SpaS for processive translocation. Notably, engineering effectors into this primed conformation bypasses the chaperone requirement for *in vivo* secretion and host invasion. These findings define a generalizable prime-and-trigger mechanism that couples host-derived signals to chaperone-mediated activation, ensuring precise spatio-temporal control of T3SS effector delivery.

Significance Statement

Protein secretion by the Type three secretion system (T3SS) underlies the virulence of many major bacterial pathogens, yet how effectors are unfolded and licensed for translocation precisely upon host contact is a longstanding mystery. This study reveals a two-step “prime-and-trigger” mechanism in which cognate chaperones actively destabilize effectors into a metastable state, while host-cell attachment generates a localized acidic microenvironment that triggers unfolding at the secretion apparatus. We further show that the gatekeeper SpaS selectively recognizes unfolded polypeptide segments and promotes directional, processive translocation. By demonstrating that engineered “pre-primed” effectors bypass the chaperone requirement in vivo, this work redefines chaperones as conformational primers rather than passive escorts and establishes how host-derived physiological signals are directly coupled to effector unfolding. These findings resolve a longstanding paradox in bacterial pathogenesis and provide a mechanistic framework for reprogramming the T3SS as a controllable protein delivery platform.

Introduction

Gram-negative bacterial pathogens use the type secretion system (T3SS), a highly conserved syringe-like nanomachine known as injectisome, to inject effector proteins directly into the cytosol of eukaryotic host cells[1–4]. This translocation event underlies many of the pathological consequences of infection, including manipulation of host signaling pathways, cytoskeletal remodeling, and immune evasion[5]. The injectisome is evolutionarily related to the flagellar basal body and is composed of a cytoplasmic sorting platform, a membrane-embedded export apparatus, and an extracellular needle that together form a continuous secretion channe[6,7]. While the structural organization and assembly of this machinery are now well established, how secretion is initiated and coordinated at the molecular level remains less clear.

Upon host-cell contact, the T3SS executes a strictly ordered secretion program[8,9]. Pore-forming translocators are secreted first to establish a conduit across the host membrane, followed by the delivery of effector proteins into the host cytosol. This initiation and hierarchy are enforced at the cytoplasmic gate, where the machinery must reconcile a profound biophysical conflict. To transit through the narrow (~ 25 Å) central channel of the needle, globular effectors must be reversibly unfolded[10–12]. Yet, unlike substrates of the Sec pathway, T3SS effectors are stably folded in the bacterial cytosol though shows mechanical labile[12,13]. This requirement for spatial and temporal precision implies that unfolding must be actively licensed at the export gate itself. Although extracellular conditions such as pH modulate T3SS activity[14], physiological effector secretion is uniquely coupled to direct host-cell contact through a unknown signal and mechanism[15].

How this signal is transduced into the energy required for unfolding is not well understood[16]. Early models emphasized a central role for the conserved T3SS ATPase in driving substrate unfolding and translocation[17]. However, secretion can proceed efficiently in the absence of ATP hydrolysis, and in some systems even without the ATPase itself[18–20]. In contrast, the proton motive force (PMF) across the inner membrane is strictly required for secretion in all systems examined[21]. Given the rapid rates of substrate export reported for many effectors, ATPase activity alone appears insufficient to account for the energetic demands of processive unfolding and transport[22–24]. These findings suggest that a complementary, probably PMF-linked mechanism must exist to catalyze the massive energetic barrier of effector unfolding and engaging precisely at the moment of host-cell attachment, and several substrates can be exported efficiently in the absence of their cognate chaperones.

T3SS effectors share a modular organization consisting of an N-terminal secretion signal, a chaperone-binding domain (CBD), and a C-terminal globular effector domain[12,25,26]. Cytosolic chaperones bind the non-globular CBD[27–29], and function as escorts that prevent premature aggregation and facilitate substrate delivery to the secretion machinery[4,28,30,31]. However, the presence of a secretion signal alone is insufficient to ensure translocation: many proteins bearing valid signals fail to be secreted[11,30,32–34], and several substrates can be exported efficiently in the absence of their cognate chaperones[35]. These observations point to a conformational checkpoint that evaluates substrate structural state rather than primary sequence, but the molecular basis of this checkpoint and its integration with energy transduction remain poorly defined.

Here, we identify the physiological signal that couples host-cell contact to effector unfolding and translocating. Using live-cell pH imaging, we show that host attachment generates a sharply localized acidic microenvironment at the cytoplasmic face of the export apparatus, driven by PMF-derived proton flux. Structural, biophysical, and computational analyses reveal a prime-and-trigger mechanism in which chaperones actively destabilize effector architecture to produce a metastable, pH-sensitive intermediate. Acidification then activates a histidine-based sensor network that catalyzes unfolding and enables segment-by-segment capture by the gatekeeper SpaS, initiating directional translocation. This mechanism selectively licenses cargo effectors while differentially regulating translocators, providing a

biophysical basis for secretion hierarchy. Together, these findings define how a host-derived physiological cue is integrated with chaperone-mediated priming to achieve precise control of protein transport through a membrane-embedded nanomachine.

Results

Host contact triggers local acidification of the T3SS export apparatus to license effector unfolding and targeting

A defining constraint of type secretion is that cytoplasmic effector proteins must unfold to pass through the narrow secretion channel (Fig. 1a, Supplementary Fig. 1a, b). Although translocation is powered by the proton motive force (PMF), how effector unfolding is spatially restricted to the export apparatus during host engagement has remained unclear.

To determine the signal that host contact generates at the T3SS export apparatus, we engineered a *Salmonella* strain expressing a ratiometric, pH-sensitive fluorescent probe (pHluorin)[36] fused to the cytoplasmic C terminus of the inner membrane export apparatus component InvA, positioning the sensor at the cytosolic face of the T3SS (Fig. 1b). Under broth culture conditions, in which the T3SS is inactive, the local pH reported at InvA was near neutral (pH 7.09 ± 0.25), closely matching the bulk cytosolic pH measured using a cytosolic pHluorin control (pH 7.42 ± 0.24) (Fig. 1c, d, Supplementary Fig. 1c-e). In contrast, upon host cell contact—a condition that activates secretion—we observed a pronounced and sustained acidification specifically at the InvA-pHluorin reporter, reaching a stable set point of pH 5.64 ± 0.17 (Fig. 1c, d, Supplementary Fig. 1e). This acidification was eliminated by the protonophore FCCP (pH 7.08 ± 0.14), indicating that it arises from PMF-dependent proton accumulation (Fig. 1c, d, Supplementary Fig. 1e). This pH change was spatially restricted to the export apparatus and did not reflect a global cytosolic acidification, demonstrating that host engagement generates a spatially confined acidic microenvironment at the T3SS export apparatus.

To reveal how this localized acidification influences effector and secretion competence, we performed thermal shift assays to assess the pH-dependent stability of multiple chaperone–effector complexes, including SigE–SopB, SicP–SptP, InvB–SopA, and InvB–SipA. In all cases, the assembled chaperone–effector complexes exhibited a steep, cooperative loss of thermal stability as pH decreased (Fig. 1e, Supplementary Fig. 2a, b). At pH values below ~ 5.5, the melting temperatures (Tm) of the complexes dropped below physiological temperature (37°C), whereas the corresponding chaperones or effectors alone remained thermally stable across the same pH range (Fig. 1e-g, Supplementary Fig. 2c, d). For example, the Tm of the SigE–SopB complex decreased from 44.5 ± 0.04°C at pH 7.0 to 34.8 ± 0.02°C at pH 5.5, while both SigE and SopB individually retained Tm values above 40°C. These results indicate that under invasion-relevant conditions, acidic pH selectively destabilizes the chaperone-bound effector complex, driving partial unfolding while preserving chaperone association.

This destabilization did not arise from dissociation of the complex. Isothermal titration calorimetry revealed that chaperone–effector binding affinities remained tight and largely unchanged between pH 6.0 and 8.0 (Fig. 1h, Supplementary Fig. 3), indicating that acidification induces conformational destabilization without disrupting chaperone binding. The consistent behavior observed across multiple, unrelated chaperone–effector pairs suggest a conserved mechanism in which chaperone binding renders effectors conditionally labile rather than stably folded.

To test whether this acid-induced destabilization licenses substrate engagement by the T3SS export gate, we used solution-state NMR to examine interactions between the cytosolic gatekeeper SpaS (SpaSc, residues 217–356) and chaperone–effector complexes. At neutral pH (7.5), SpaS showed no detectable interaction with stable SigE–SopB, SicP–SptP, InvB–SipA, or InvB–SopA complexes (Supplementary Fig. 4a). In contrast, under acidic conditions (pH 5.5), or at elevated temperature (40°C) that mimics thermal destabilization, SpaS engaged robustly with the chaperone–effector complexes, as evidenced by pronounced chemical shift perturbations and peak broadening (Supplementary Fig. 4b, c). Thus, SpaS selectively recognizes a destabilized or partially unfolded chaperone-bound effector state, rather than the fully folded complex (Fig. 1i).

Together, these findings define a coherent physiological pathway for effector licensing (Fig. 1i). Host cell contact generates a localized acidic signal at the T3SS export apparatus that selectively destabilizes chaperone–effector complexes without disrupting their association. This primed, partially unfolded state is specifically recognized by the export gatekeeper SpaS, thereby coupling host-derived environmental sensing to effector targeting and commitment to translocation.

Structural basis for chaperone-mediated priming and pH-sensitive unfolding of SopB

Our biophysical analyses indicated that chaperone binding converts effectors into a selectively acid-labile state. To define the structural basis of this priming mechanism, we performed an integrated biochemical and structural dissection of a representative chaperone-substrate complex, SigE-SopB. SopB exhibits the canonical T3SS effector architecture, with an N-terminal chaperone-binding domain (CBD) followed by a C-terminal phosphatase domain (PD) (Supplementary 5a). Consistent with this organization, SigE binds exclusively to the CBD (Supplementary 5b, c). This binding induced a pronounced shift in SopB's oligomeric state from a high-order oligomer (~ 350 kDa) to a lower oligomeric form (~ 240 kDa) (Supplementary 5d). SigE binding also increased SopB phosphatase activity and enhanced aggregation propensity (Supplementary 5e, f), indicating that engagement at the CBD propagates long-range conformational or dynamic changes that decouple catalytic competence from structural stability. Moreover, the SigE–SopB complex exhibited progressive pH-dependent destabilization and de-oligomerization without dissociation of the complex (Supplementary 5g), suggesting that chaperone binding generates a metastable architecture poised for environmental triggering. To visualize this remodeling at near-atomic resolution, we determined cryo-EM structures of

SopB in its chaperone-free and SigE-bound states across a physiological pH range (pH 8.0, 7.0, and 6.0) (Fig. 2a, b, Supplementary Fig. 6, Supplementary Table 1–2).

In the absence of chaperone, SopB assembled into a rigid, double-layered homohexamer at all tested pH values (Fig. 2a, Supplementary 7a, b). Structures determined at pH 8.0 and 7.0 were essentially identical (2.62 Å and 3.10 Å resolution, respectively), indicating strong intrinsic stability. At pH 6.0, only partial destabilization was observed: while the CTD remained well ordered, density corresponding to the CBD weakened or disappeared in four of six subunits, consistent with localized flexibility rather than global unfolding (Fig. 2a). Thus, mild acidification is insufficient to disrupt the SopB core structure.

Chaperone binding fundamentally altered this behavior. At pH 8.0, the cryo-EM structure of the SigE–SopB complex (2.9 Å) revealed that SigE dimers engage the CBD and dismantle the double-layered hexamer into a single layer of SopB trimers (Fig. 2b, Supplementary Fig. 6b, Supplementary Fig. 7c, d, Supplementary Table 2). This rearrangement eliminates the stabilizing inter-trimer interface, yielding a trimeric assembly with increased intrinsic dynamics. Acidification amplified this instability. At pH 7.0, the SigE–SopB complex exhibited increased conformational heterogeneity, reflected by reduced map resolution (3.6 Å) and partial loss of density for one SopB subunit and its associated SigE dimer (Fig. 2b, Supplementary Fig. 6b, Supplementary Table 1). At pH 6.0, particle heterogeneity became extreme, precluding high-resolution reconstruction; reference-free 2D class averages showed diffuse, featureless particles consistent with global unfolding (Fig. 2c, Supplementary Fig. 6b). Particle yields decreased sharply with lowering pH, an effect substantially more pronounced for the SigE–SopB complex than for SopB alone **(**Fig. 2c, **Supplementary Fig. 6).** Together, these observations demonstrate that chaperone binding is required to render SopB acutely sensitive to acid-induced structural collapse.

Structural comparison revealed that neither chaperone binding nor acidification perturbs the fold of the PD, which remains rigid across all conditions except at pH 6.0 in the SigE–SopB complex. Instead, priming arises from reorientation of the CBD relative to the PD by ~ 10° and liberation of a flexible hinge loop (residues 520–539) connecting the two domains (Fig. 2d-e, Supplementary Fig. 7e). Both regions exhibited markedly elevated B-factors in the SigE-bound state and showed the strongest pH-dependent increases in dynamics (Fig. 2d-e, Supplementary Fig. 7e-f). Molecular dynamics simulations corroborated these observations. The CBD and hinge loop of the SigE–SopB complex sampled extended, fluctuating conformations, whereas the chaperone-free SopB remained relatively rigid (Fig. 2e). Protonation analysis identified a cluster of histidine residues (H180, H450, H482, H485) predicted to have pKa values above the experimentally observed acidic trigger point (~ 5.6) and embed in a hydrophobic patch (Fig. 2e), indicating unfavorable interaction. These histidines are flanked by basic side chains, such that protonation would trigger electrostatic repulsion or neutralize attractive interactions (Fig. 2f, Supplementary Fig. 8a-c).

Consistent with this model, substitution of these histidines with arginine (H→R), mimicking constitutive protonation, destabilized the SigE–SopB complex even at neutral pH and markedly increased aggregation under acidic conditions (Fig. 2g-h, Supplementary Fig. 8d-e). Conversely, substitution with

aspartate (H→D), introducing a stabilizing negative charge, rescued complex stability at low pH and suppressed aggregation (Fig. 2h). These results identify histidine protonation as the chemical switch that converts chaperone-mediated priming into reversible unfolding.

Together, these data define a two-step structural mechanism for pH-sensitive effector activation. Chaperone binding first primes SopB by dismantling stabilizing oligomeric interfaces and liberating a flexible interdomain hinge, generating a metastable architecture. Localized acidification then protonates a dedicated histidine network exposed by this priming, triggering structural collapse. This mechanism provides a direct structural explanation for how environmental pH cues are integrated with chaperone binding to license effector unfolding during type III secretion.

Chaperone binding destabilizes SopB by rewiring oligomeric and intramolecular hydrophobic networks

Our biophysical and MD simulation analyses indicated that the N-terminal chaperone-binding domain of SopB is flexible, whereas the isolated C-terminal phosphatase domain is sensitive to acidic pH. In contrast, full-length SopB is remarkably stable, suggesting that intramolecular and oligomeric interactions collectively buffer the effector against unfolding. Contrast to this, the remaining trimer–trimer contacts are highly identical between SopB and SigE bound SopB, which mediated largely by salt bridges and are intrinsically fragile: modest perturbations, including single-point mutations, changes in ionic strength, or mild pH shifts, readily destabilized the trimeric organization (Supplementary Fig. 5g, Supplementary Fig. 9). Moreover, whereas apo SopB assembles as a double-layered hexamer composed of two stacked trimers, the SigE-bound complex contains only a single trimeric layer, further indicating that chaperone binding reduces oligomeric robustness. We therefore sought to define, at atomic resolution, how chaperone binding remodels stabilizing interaction networks to prime SopB for unfolding.

Cryo-EM analysis revealed that apo SopB assembles as a homohexamer composed of two face-to-face trimers (Fig. 3a), whereas the SigE–SopB complex forms a single trimeric layer (Fig. 3b). In the apo hexamer, stability is dominated by an extensive hydrophobic inter-trimer interface. Antiparallel hairpin loops from opposing trimers (residues 304–314, 360–371, and 525–537) interdigitate to form a dense hydrophobic core centered on residues I309, F310, L364, L368, F370, and L535 (Fig. 3c). This interlocking network generates a rigid oligomeric scaffold that accounts for the remarkable stability of full-length SopB across a broad pH range.

Binding of the cognate chaperone SigE profoundly alters this architecture. Rather than reinforcing oligomerization, SigE dismantles the SopB hexamer into a single trimer, with each SopB subunit bound by a SigE homodimer to form a hetero-nonameric complex (Fig. 3b). Structural inspection shows that SigE occupies the same surface used for inter-trimer packing in the apo hexamer. Notably, however, this SigE–SopB interface itself is unexpectedly sparse comparing to the hexamer interface, comprising only two hydrophobic contacts (F310–P45 and L535–I24), with SopB binding mediated dominantly by a

flexible loop region of SigE (residues 30–69) (Fig. 3c-d). Consistent with this, mutations that weaken the SopB hexameric interface (I309G, F310G, L364G, L368G, F370G, L535G) destabilize the hexamer and shift SopB to a trimeric state (Fig. 3e), whereas mutations at this interface or corresponding SigE residues (Y32G, P45G, P45I) have minimal effects on SigE binding affinity (Fig. 3f, Supplementary Fig. 10a-c). These observations indicate that SigE does not dissociate the hexamer through stronger competitive binding, but instead induces more global conformational rearrangements.

At the center of this reorganization is the hinge loop, which acts as a mechanical coupling element linking oligomerization to intramolecular domain packing (Fig. 2d, 3g-h). In the chaperone-free state, this hinge either contributes directly to the inter-trimer interface (L535) or packs against the PD, with V526 and M527 inserting into a hydrophobic pocket of the globular domain (Fig. 3g-h). Upon SigE binding, the hinge loop undergoes a dramatic reorientation, disengaging from both the hexamer interface and the PD pocket (Fig. 2d-f, 3g-h). Instead, it adopts an exposed conformation positioned between the CBD and PD, without forming compensatory stabilizing contacts (Fig. 3h).

This hinge relocation has a critical secondary consequence: it disrupts a hydrophobic interface between the CBD and PD. In apo SopB, hydrophobic residues L76, L79, and L83 in the CBD pack tightly against I555, L558, and I559 in the PD, locking the two domains into a compact, stable arrangement (Fig. 3g). SigE binding induces a helix-to-loop transition in the L76–L83 region, abolishing these contacts and physically separating the CBD from the PD (Fig. 3h). As a result, The PD becomes conformationally liberated and no longer shielded by the CBD.

To test whether disruption of this intradomain hydrophobic network is sufficient to destabilize SopB, we generated targeted mutants that selectively weaken the CBD–PD or hinge-PD interaction (L76G/L79G, I555G/L558G, V526G/M527G). All of these mutants phenocopied the chaperone-bound state in oligomer state, dynamic and stability: SopB shifted from a hexamer to a trimer in size-exclusion chromatography (Fig. 3i), exhibited increased conformational dynamics in molecular dynamics simulations (Fig. 3j), and displayed markedly reduced thermal stability (Fig. 3k). These mutants were also substantially more susceptible to proteolytic degradation (Fig. 3l, Supplementary Fig. 10d), demonstrating that the observed destabilization reflects an increased propensity for unfolding rather than mere oligomeric rearrangement and intrinsic dynamic change.

Collectively, these data show that SigE primes SopB by allosterically rewiring a multiscale hydrophobic interaction network that stabilizes both its oligomeric assembly and intramolecular domain packing. By dismantling these coupled stabilizing interfaces, chaperone binding converts SopB into a dynamic, metastable conformation in which the phosphatase domain is rendered accessible to the acidic trigger (Fig. 2f-h).

Structural insight into the chaperone bound states mimic mutants and processive effector translocation

Our structural analyses identified two stabilizing elements that are dismantled by chaperone binding: the inter-trimer interface that supports hexamer formation and the intramolecular interface coupling the N-terminal chaperone-binding domain (CBD) to the C-terminal phosphatase domain (PD). We reasoned that disrupting these interfaces genetically should constitutively “prime” SopB, mimicking the chaperone-bound state in the absence of SigE.

To test this, we generated two classes of SopB mutant: hexamer-disrupting mutants (I309G, F370G, L535G) and intradomain-disrupting mutants (L76/79G, V526/M527G, I555G/L558G). Cryo-EM analysis confirmed that all mutants adopted a common structural phenotype. In contrast to the stable wild-type hexamer, each mutant assembled exclusively as a trimer and lacked resolvable density for the CBD and hinge region (Fig. 4a, Supplementary Fig. 11a). Representatively, we determined the cryoEM structures of SopB F370G and SopB I555/L558G, which showed well-defined density only for the trimeric PD, with the CBD and the hinge region completely disordered (Fig. 4b-c, Supplementary Fig. 11b-c). This architecture is indistinguishable from that of the SigE–SopB complex under acidic conditions (Fig. 2b-c), indicating that these mutations generate structural mimics of the chaperone-primed state.

This structural mimicry extended to protein dynamic properties. Structural comparison analysis demonstrated that the F370G and I555G/L558G mutants exhibited flexibility profiles nearly superimposable with the SigE-SopB complex, with pronounced dynamics in the CBD and hinge region (Fig. 2e, Fig. 4d, Supplementary Fig. 12a-c). Upon mild acidification (pH 6.0), particle heterogeneity increased sharply, mirroring the acid-induced unfolding observed for the chaperone-bound complex (Fig. 2c, Fig. 4e). Thus, disruption of either stabilizing interface is sufficient to generate a metastable, acid-sensitive effector conformation.

To further validate the mimic prime state, we tested if the interface-disrupted mutants retain the intrinsic pH-sensing mechanism identified. In both wild-type SopB and the primed-state mimics, key histidine residues within the PD (H180, H263, and H482) remained structurally ordered and engaged in long-range interactions with surrounding basic residues, forming a series of pH-sensing spots (Fig. 4f, Supplementary Fig. 12d). Consistent with this, the F370G and I555G/L558G mutants displayed melting temperatures near physiological temperature (37°C), closely matching those of the SigE-bound wild-type protein and confirming effective priming. Substitution of these His sensor residues with aspartate or glutamate (H→D/E), increased overall stability (Fig. 4g, Supplementary Fig. 12d) and suppressed aggregation both at pH 8.0 and pH 6.0 (Fig. 4h). In contrast, histidine-to-arginine substitution (H→R) mutations, mimicking constitutive protonation, increased low-pH aggregation (Fig. 4h). These histidine residues lie outside the catalytic center, and phosphatase activity was preserved unless histidines were substituted with arginine, directly linking protonation-driven destabilization to structural collapse and subsequent loss of enzymatic function (Fig. 4i). These results demonstrate that the PD’s intrinsic pH sensitivity is revealed only when its stabilizing interfaces are disrupted, either by chaperone binding or by designed mutation.

We next examined whether constitutive priming alone is sufficient to license SopB for engagement by the T3SS export gatekeeper. Using solution-state NMR spectroscopy, we examined interactions between SopB variants and the cytosolic domain of the export gatekeeper SpaS. At neutral pH (7.5), SpaS showed robust binding to the F370G and I555G/L558G mutants—an interaction that, for wild-type SopB, was observed only under acidic conditions and in the presence of SigE (Supplementary Fig. 13a-b). Binding increased further upon acidification, consistent with progressive exposure of unfolded polypeptide segments (Supplementary Fig. 13a-b). In contrast, SpaS did not interact with SigE alone (Supplementary Fig. 13c) or with a folded SopB variant lacking the N-terminal disordered signal region (SopB Δ29) (Supplementary Fig. 13d). Notably, SpaS bound to multiple short, SopB fragments spanning the length of the protein, confirming its preference for unfolded polypeptide segments rather than a specific folded domain (Supplementary Fig. 13e-j). Together, these data demonstrate that disruption of SopB's stabilizing interaction network is sufficient to generate a substrate that is competent for recognition by the T3SS export gatekeeper. Chaperone binding is therefore not required for gate engagement itself, but instead functions to produce a primed, unfolding-prone effector state that is segment-by-segment captured by SpaS to initiate processive translocation (Fig. 4j).

Chaperone bound state mimic mutants lead to effector secretion and host invasion in chaperone free T3SS

To establish the functional importance of this prime-and-trigger mechanism *in vivo*, we sought to test secretion and invasion using a designed genetic complementation system (Fig. 5a). In a ΔsopB strain, in which the endogenous chaperone SigE is present, all interface-disrupting SopB mutants—targeting either the hexameric interface (I309G, F310G, L364G, F370G, L535G) or the intramolecular CBD–PD interface (L76/79G, V526/M527G, I555G/L558G)—were secreted at substantially higher levels than wild-type SopB (Fig. 5b, left, Supplementary Fig. 14a). Among these, the I555G/L558G mutant exhibited up to a fourfold increase in secretion. These results indicate that a destabilized, primed conformation constitutes an optimal secretion substrate even in the presence of the native chaperone system.

The definitive experiment was performed in a Δ*sopB*Δ*sigE* double gene knockout strain, in which SopB secretion is normally abolished due to loss of its cognate chaperone. As expected, secretion of wild-type SopB was abolished. Strikingly, the constitutively primed mutants (I309G, F310G, L364G F370G, L535G and L76/79G, V526/M527G, I555G/L558G) were robustly secreted in this chaperone-free background (Fig. 5b, right, Supplementary Fig. 14b). This demonstrates that the primed state itself, not the chaperone, is the essential licensing factor for the secretion machinery.

We then asked whether chaperone-independent secretion supports effector injection and host cell invasion. Immunofluorescence microscopy revealed that whereas translocation of wild-type SopB strictly required SigE, the F370G and I555G/L558G mutants were efficiently injected into host cells even in the ΔsigE strain (Fig. 5c-d, Supplementary Fig. 14c). Functional consequences of this delivery were assessed using quantitative adhesion and invasion assays in a ΔsopBΔsopE2 background, which eliminates compensate invasion pathways (Fig. 5e, Supplementary Fig. 15a). Under these conditions,

adhesion was not affected as expected (Fig. 5f, Supplementary Fig. 15b-c), while primed SopB mutants restored bacterial invasion to wild-type levels and did so independently of SigE (Fig. 5e-g, Supplementary Fig. 15). Notably, the I555G/L558G mutant exhibited enhanced effector injection and invasion efficiency in the presence of chaperones and fully rescued invasion in chaperone absence, consistent with its pronounced secretion phenotype (Fig. 5d, 5g, Supplementary Fig. 15). This establishes a direct causal chain linking structural priming to effector injection, and host cell invasion.

To further validate which components initiates the “prime-and-trigger” mechanism, we examined representative components from each major functional class, including the cytoplasmic domain of export apparatus proteins (InvA, SpaS), translocators (SipB, SipC), and the needle tip protein SipD (Supplementary Fig. 16a). Thermal shift analyses revealed that, like effector–chaperone complexes, the SipC–SicA translocator complex exhibited sharp, cooperative destabilization at acidic pH (Fig. 5h, Supplementary Fig. 16b-c). In contrast, SipB, SipD, and the cytosolic domains of InvA and SpaS were pH-stable (Fig. 5h, Supplementary Fig. 16d-g). This suggests a sequential activation model: initial insertion of the stable SipB may nucleate translocon formation and establish the acidic niche, which then licenses the unfolding and secretion of the pH-sensitive SipC to complete the translocon, paving the way for subsequent effector secretion.

To makes the secretion model comprehensive, we defined the directionality of effector engagement with the export apparatus. Using a secretion-trap assay with pHluorin fused to either the N- or C-terminus of SopB (Supplementary Fig. 16h), we observed that SopB C-terminally fused pHluorin was drawn into the acidic export apparatus, while an N-terminal fusion remained in the neutral cytosol (pH ~ 6.9) (Fig. 5i, Supplementary Fig. 16i). This proves translocation initiates at the N-terminus, consistent with its role in targeting, and suggests SpaS engages the unfolded polypeptide in an N-to-C direction to processively thread it into the secretion channel.

Together, our findings coalesce into a comprehensive model for the spatio-temporal control of type secretion (Fig. 5j). We propose a 'prime-and-trigger' mechanism where secretion is governed by a two-step conformational licensing process. In the bacterial cytosol, chaperones act as active conformational primers rather than passive escorts, dismantling internal stabilizing networks to render effectors metastable. This 'primed' state is selectively activated upon host contact, which triggers a PMF-derived proton flux that creates a localized acidic microenvironment (pH 5.6) at the export gate. Crucially, this acidic signal acts as a biophysical switch: while the first translocator, SipB, remains pH-insensitive to ensure initial pore formation, the subsequent translocator, SipC, and cargo effectors undergo rapid histidine-mediated unfolding in response to acidification. These unfolded intermediates are captured by the gatekeeper SpaS, which facilitates directional, N-to-C threading through the secretion channel. By directly coupling host-derived physiological cues to substrate stability, this mechanism resolves the long-standing paradox of how the injectisome achieves rapid, processive protein transport with exquisite temporal precision. More broadly, our ability to bypass chaperone requirements through 'pre-primed' effectors establishes conformational priming as a fundamental principle for regulated transport across membrane-embedded gates.

Discussion

The Type Ⅲ Secretion System (T3SS) has long posed a fundamental biophysical paradox: effector proteins must be fully unfolded to traverse the narrow secretion channel, yet premature unfolding in the bacterial cytoplasm would be catastrophic. How this decisive conformational transition is licensed precisely at the moment of host contact has remained unresolved. Here, we identify the missing trigger. We show that host-cell attachment generates a sharply localized acidic microenvironment (pH ~ 5.6) at the cytosolic face of the export apparatus and that this host-derived signal directly catalyzes effector unfolding. Crucially, this acidification acts only on effectors that have been preconditioned by their cognate chaperones. Together, these findings define a “prime-and-trigger” mechanism that spatially and temporally confines effector unfolding to the host–pathogen interface.

Our direct visualization of localized acidification fills a critical gap in current models of T3SS activation. While the proton motive force (PMF) has been implicated in energizing secretion[19] and extracellular pH has been linked to regulatory control of T3SS components[14], a compartmentalized physiological signal coupling host contact to substrate unfolding was missing. The spatial restriction of this acidic niche ensures that only effectors docked at the export gate are unfolded, preventing futile unfolding in the cytoplasm. This mechanism operates independently of the cytosolic ATPase, providing a coherent explanation for ATPase-independent secretion[18] and revealing PMF-driven proton accumulation as a direct unfolding trigger rather than merely an energy source.

A central conceptual advance of this work is the redefinition of chaperone function in the T3SS. Through integrated structural and biophysical analysis of the SopB–SigE complex, we show that chaperone binding actively dismantles effector stability by disrupting key oligomeric and interdomain interfaces. This converts a stable homohexamer into a dynamic, monomeric complex, exposing electrostatic networks centered on critical histidine residues. The chaperone thus installs a molecular pH sensor: protonation of these histidines under acidic conditions introduces electrostatic repulsion that catalytically unfolds the already-weakened structure. In this light, chaperones are allosteric primers, converting effectors from stable cellular proteins into conditionally labile secretion substrates.

The definitive proof of this priming mechanism lies in our ability to genetically engineer secretion competence. Mutations that disrupt the same stabilizing interfaces targeted by chaperones (e.g., F370G, I555G/L558G) constitutively generate a primed, pH-sensitive effector state. These engineered substrates are secreted and translocated into host cells in the complete absence of their cognate chaperone and restore bacterial invasion. This genetic bypass provides definitive proof that the primed conformation itself—not the chaperone protein—is the essential licensing factor recognized by the secretion machinery. This finding provides a unifying principle for the diversity of effector-chaperone relationships observed in nature. While effectors natively exist in a chaperone-independent secretion also converge on the same structural endpoint: a metastable, pH-labile conformation[37,38] that is licensed for acid-triggered unfolding and translocation. Our findings unify diverse observations: whether an effector natively exists

in a primed state or requires chaperone-mediated priming, each converges on the same acid-triggered unfolding pathway prior to translocation.

A particularly important implication of our findings is the redefinition of how the T3SS gatekeeper SpaS recognizes secretion substrates. We show that SpaS does not bind folded effectors, isolated chaperones, or stable chaperone–effector complexes. Instead, SpaS selectively engages effectors only when they are partially unfolded, either through chaperone-mediated priming under acidic conditions or through engineered destabilization. Remarkably, SpaS binds multiple short, unstructured fragments distributed across the effector sequence, indicating that recognition is governed by folding state rather than primary sequence. This multivalent engagement provides a mechanistic explanation for how SpaS functions simultaneously as a specificity filter, a positional anchor, and a processivity factor. By stabilizing exposed polypeptide segments and preferentially engaging the N-terminus, SpaS can promote directional, N-to-C threading of the unfolded substrate into the secretion channel, ensuring efficient and irreversible translocation.

The “prime-and-trigger” logic uncovered here appears to be broadly generalizable. We find that the translocator SipC, in complex with its chaperone SicA, exhibits a similar pH-dependent destabilization, whereas other substrates such as SipB and the needle-tip protein SipD remain pH-stable. This suggests a hierarchical activation model in which initial insertion of stable translocon components establishes the acidic niche that subsequently licenses unfolding and secretion of pH-sensitive substrates. Such a mechanism provides temporal order to translocon assembly and effector.

In summary, we define a coherent physicochemical pathway that explains how T3SS effectors are unfolded, recognized, and translocated with spatial and temporal precision. Chaperones prime effectors into a metastable state, host contact generates a localized acidic trigger, and the gatekeeper SpaS selectively engages the unfolded substrate to drive processive secretion. By resolving how environmental sensing, conformational priming, and substrate recognition are integrated at the molecular level, this work establishes a general framework for bacterial protein injection and provides a foundation for reprogramming the T3SS as a programmable protein delivery platform.

Methods

Bacterial Strains, Plasmids, and Growth Conditions

All *Salmonella enterica serovar Typhimurium* strains used in this study are isogenic derivatives of the wild-type strain LT2 (SGSC1412 / ATCC 700720). *Escherichia coli* strains DH5α and BL21(DE3) served as hosts for cloning and recombinant protein expression, respectively.

For molecular genetics and complementation studies in *Salmonella*, genes were expressed from the arabinose-inducible pBAD3 vector or the IPTG-inducible pTrc99a vector. Chromosomal gene deletions were generated using the λ-Red recombinase system with plasmids pKD46 (encoding recombinase functions) and pKD3 or pKD4 (template for antibiotic resistance cassettes). For in vitro studies, proteins

were expressed from pET-derived vectors: the chaperone-effector complex was co-expressed from pETDuet-1, and individual proteins were expressed from pET15b. All strains, plasmids, and oligonucleotide sequences are detailed in Supplementary Table 4.

For routine propagation, strains were grown aerobically at 37°C in Luria-Bertani media (LB). Protein expression cultures were grown in Terrific Broth (TB) or in M9 minimal medium (6.8 g/L Na_2HPO_4, 3.0 g/L KH_2PO_4, 0.5 g/L NaCl, 1.0 g/L NH_4Cl) supplemented with 4 g/L glucose, 0.25 g/L $MgSO_4$, 0.01 g/L $CaCl_2$, and 0.01% (w/v) vitamin B. For isotopic labeling of proteins for NMR, M9 medium was prepared with 1 g/L [U-^{15}N]-NH_4Cl (Cambridge Isotope Laboratories) as the sole nitrogen source. Antibiotics were used at the following concentrations: ampicillin, 100 μg mL^{-1}; chloramphenicol, 25 μg mL^{-1}.

Strain Construction and Genetic Manipulations

Chromosomal gene deletions in *Salmonella Typhimurium* were generated using the λ-Red recombinase system. In brief, linear DNA fragments containing an FRT-flanked chloramphenicol resistance cassette, amplified with primers (Supplementary Table 1) bearing 50-nucleotide homology arms, were electroporated into strains expressing the red recombinase from plasmid pKD46. Recombinants were selected on LB agar containing chloramphenicol. Successful allelic exchange was confirmed by PCR. The resistance cassette was subsequently excised by FLP recombinase expressed from plasmid pCP20 to create unmarked, scarless deletions, after which both helper plasmids were cured. Using this method, we constructed a clean *sopb*$^-$ *single gene knockout strain*, *sopb*$^-$*/sige*$^-$ double knockout mutant. The double knockout strain served as the parent for generating the *sopb*$^-$*/sige*$^-$*/sope2*$^-$ triple mutant, as well as the base strain for all complementation studies. For genetic complementation, the native *sopb* and *sige* genes (or their mutant variants) were cloned into the arabinose-inducible pBAD3 or the IPTG-inducible pTrc99a vector. Gene expression was induced with 0.1% (w/v) L-arabinose or 50 μM IPTG, respectively. Site-directed mutagenesis was performed using the QuikChange protocol (Agilent Technologies). The sequence of every cloned insert and all engineered mutations was verified by further sequencing.

Recombinant Protein Expression and Purification

All the genes of the proteins in this study were derived from *Salmonella Typhimurium* STM1913/700720 (ATCC). The DNA sequences encoding all the proteins were amplified with PCR and then inserted into pETDuet-1 or pET15b vectors. Proteins for *in vitro* studies were expressed in *Escherichia coli* BL21(DE3). Constructs for chaperone-substrate complexes, including SigE-SopB, SicP-SptP, InvB-SipA, InvB-SopA, SicA-SipB, and SicA-SipC, were generated using the pETDuet-1 vector. In each case, the gene encoding the chaperone with an N-terminal 6xHis tag was inserted into the first multiple cloning site, and the gene for its cognate substrate was inserted into the second site. For expression of the effector SopB and its derivatives—including the signal peptide deletion mutant (SopBΔ29, residues 30–561), other truncations, and site-directed mutants—the corresponding genes were cloned into a modified pET15b vector

encoding an N-terminal 6xHis-MBP tag followed by a TEV protease cleavage site. The same vector was used for other T3SS components: the cytosolic domain of the small export gate protein SpaS (SpaSc, residues 217–356), the cytosolic domain of the large export gate protein InvA (InvAc, residues 357–685), and the tip protein SipD. Expression of these proteins was induced with 0.5 mM IPTG when cultures reached an OD_{600} of 0.6–0.8, followed by incubation for 16–18 h at 18°C.

Cells were harvested by centrifugation (5,000 × g, 10 min, 4°C) and lysed by a pressure homogenizer in Buffer A (20 mM Tris-HCl pH 8.0, 150 mM NaCl, 20 mM imidazole, 1 mM PMSF). Clarified lysates were loaded onto Ni^{2+}-NTA affinity resin (Qiagen), washed extensively with Buffer A, and eluted with Buffer B (20 mM Tris-HCl pH 8.0, 150 mM NaCl, 500 mM imidazole). For proteins bearing the 6xHis-MBP tag, the tag was removed by incubation with TEV protease overnight at 4°C, followed by reverse immobilization on Ni^{2+}-NTA resin to separate the cleaved protein from the tag, protease, and intact protein. Chaperone-substrate complexes were purified intact via the 6 x His tag on the chaperone. All proteins were further purified by size-exclusion chromatography on a HiPrep 26/60 Sephacryl S200 HR column (Cytiva) equilibrated with 20 mM HEPES pH 7.5, 150 mM NaCl. Purity and oligomeric state were assessed by SDS-PAGE and analytical size exclusion chromatography.

Protein isotope labeling and NMR titration

Uniformly ^{15}N-labeled samples of the SpaS cytosolic domain (SpaSc, residues 217–356) were produced for NMR analysis. For expression, *E. coli* BL21(DE3) harboring the pET15b SpaSc expression plasmid was grown in M9 minimal medium containing 1 g/L [U-^{15}N]-NH_4Cl (Cambridge Isotope Laboratories) as the sole nitrogen source. Protein expression was induced at an OD_{600} of 0.9 with 0.5 mM IPTG, and cultures were incubated for 24 h at 16°C before harvest. Purification of isotopically labeled SpaSc followed the same protocol as for unlabeled proteins, with a final buffer exchange into NMR storage buffer (50 mM sodium phosphate, pH 7.5 or pH 5.5, 150 mM NaCl, 0.05% NaN_3).

NMR experiments were performed at 25 ℃ or 40 ℃ on Bruker AVANCE III spectrometers operating at ^1H frequencies of 600 MHz or 800 MHz, each equipped with a cryogenically cooled probe. For binding studies, a series of 2D ^1H-^{15}N HSQC (Heteronuclear Single-quantum Correlation) spectra were acquired for 0.2 mM ^{15}N-labeled SpaSc titrated with 0.02 mM of unlabeled proteins. These included substrate proteins alone, their cognate chaperones, pre-formed chaperone-substrate complexes, and various SopB truncations or mutants. Titrations were conducted at specified pH values (pH 5.5 or pH 7.5) as well as specific temperature (at 25 ℃ or 40 ℃) to assess pH-dependent interactions. Spectra were processed using NMRPipe and analyzed with Sparky and NMRViewJ.

Fluorescent Dye-Monitored Thermal Shift Assays

Thermal shift assays (also known as differential scanning fluorimetry) were performed to determine the thermal stability of proteins under different conditions, adapting a previously established protocol[39]. Briefly, protein samples containing 5 μM purified protein samples (monomer concentration) were

prepared in 20 µL of 20 mM sodium phosphate (pH 7.5), 150 mM NaCl. For pH-dependent measurements, the buffer was adjusted to the specified pH using 20 mM sodium acetate (pH 4.5–7.0) or sodium phosphate (pH 7.0–8.5), all containing 150 mM NaCl. Immediately prior to measurement, 5 µL of a 1000× dilution of SYPRO® Orange protein gel stain (Invitrogen, S6650) in the same assay buffer was added to each sample, resulting in a final dye dilution of 10,000× in a total volume of 25 µL. Samples were loaded into a 96-well hard-shell PCR plate (Bio-Rad, HSP9601), sealed with optically clear film, and centrifuged. Thermal denaturation was monitored using a CFX96 Touch Real-Time PCR Detection System (Bio-Rad). The temperature was increased from 20°C to 55°C at a rate of 0.5°C per 20-second interval, with a fluorescence measurement taken at each step. Fluorescence was detected using the instrument's FRET channel, corresponding to excitation at 490 nm and emission detection at 575 nm. Raw fluorescence data were plotted as a function of temperature. The melting temperature (Tm), defined as the inflection point of the unfolding transition, was determined by fitting the data to a Boltzmann sigmoidal model using OriginPro 8.5 (OriginLab)[40].

Isothermal Titration Calorimetry

Isothermal titration calorimetry (ITC) experiments were performed to quantify the binding affinity and thermodynamics of chaperone-substrate interactions. Measurements were carried out using a MicroCal PEAQ-ITC instrument (Malvern Panalytical) at 25°C (298 K). All proteins were dialyzed extensively into matching degassed buffers: either 20 mM sodium phosphate, 150 mM NaCl (pH 8.0) or 20 mM sodium acetate, 150 mM NaCl (pH 6.0). For a standard titration, the sample cell was loaded with 20 µM substrate protein (e.g., MBP-tagged SopB or its mutants). The injection syringe was filled with 200 µM of the cognate chaperone (e.g., SigE) in the same buffer. Titrations consisted of an initial 0.4 µL injection (discarded from the analysis) followed by 15 subsequent injections of 2.0 µL each, spaced 150 seconds apart, with a constant stirring speed of 750 rpm. Control experiments, in which the chaperone was titrated into buffer alone, were performed in identical fashion to measure and subtract the heat of dilution. All titrations were performed in triplicate using independently prepared protein samples. Data were processed and analyzed using the MicroCal PEAQ-ITC Analysis software. The integrated heat peaks were fitted to a single-site binding model to obtain the dissociation constant (K_D), enthalpy change (ΔH), and binding stoichiometry (N).

Protease Susceptibility Assay

Protease sensitivity activity was assessed to probe the structural integrity and unfolded state of SopB and its variants. Purified proteins—including wild-type SopB and engineered mutants—were buffer-exchanged into assay buffer (20 mM Tris-HCl pH 8.0, 150 mM NaCl, 5 mM $MgCl_2$) and concentrated to 2 mg/mL. Subtilisin A from *Bacillus licheniformis* (Protease Type VIII, Sigma-Aldrich) was prepared as a 10 U/mL stock solution in the same assay buffer immediately before use. For each digestion, 20 µL of protein sample was incubated with 5 µL of subtilisin at final concentrations ranging from 0.5 to 5.0 U/mL on ice for 30 minutes. A control sample without protease was included for each protein. Reactions were terminated by adding 6 µL of 5× SDS-PAGE loading buffer (310 mM Tris-HCl pH 6.8, 10% SDS, 50% glycerol, 0.05% bromophenol blue, 500 mM DTT) and heating at 100°C for 5 minutes. Samples were

resolved on 4–20% gradient Tris-glycine polyacrylamide gels (Bio-Rad) and stained with Coomassie Brilliant Blue R-250. Gel images were acquired using a ChemiDoc MP Imaging System (Bio-Rad). The intensity of the full-length protein band in each lane was quantified using Fiji/ImageJ software and normalized to the intensity of the corresponding no-protease control. The fraction of intact protein remaining was plotted against subtilisin concentration. Each condition was tested in three independent experiments.

Turbidity Assay for pH-Dependent Aggregation

Protein aggregation as a function of protein unfolding was assessed by monitoring solution turbidity. Purified proteins were dialyzed into a base buffer of 150 mM NaCl and concentrated to a stock concentration of 200 µM. For the assay, proteins were diluted to a final concentration of 20 µM (monomer) in a series of 20 mM sodium phosphate buffers pre-adjusted to specific pH values (ranging from pH 5.0 to 8.0 in 0.2–0.5 pH unit increments) containing 150 mM NaCl. Samples (200 µL) were prepared in triplicate in a clear, flat-bottomed 96-well plate (Corning) and incubated at 25°C for 15 minutes to equilibrate. The absorbance at 340 nm (A_{340}), which reports on light scattering due to protein aggregation, was then measured for each well using a SpectraMax M5 microplate reader (Molecular Devices). The mean absorbance value from three replicate wells was calculated for each condition. Buffer-only blanks at each pH were subtracted from the sample readings.

Phosphatase Activity Assay

The phosphoinositide phosphatase activity of SopB and its mutants was quantified using a discontinuous malachite green assay that detects inorganic phosphate (Pi) release. The short-chain diC8-PtdIns (3,4,5) P_3 (Echelon Biosciences) was used as a water-soluble substrate. Reactions were performed in 30 µL volumes in assay buffer (100 mM Tris-HCl pH 7.5, 1 mM $MgCl_2$, 0.1 mg/mL bovine serum albumin). Purified SopB protein and its mutants were added to a final concentration of 20 nM, and reactions were initiated by adding the lipid substrate to a final concentration of 300 µM. The reaction mixture was incubated at 37°C. At designated time points 30 min, 2–5 µL aliquots were withdrawn and the reaction was immediately quenched by mixing with 2–5 µL of 1 N HCl in a separate 96-well plate. To detect released phosphate, 10 µL of a freshly prepared malachite green reagent (0.034% malachite green oxalate, 1.05% ammonium molybdate in 1 N HCl, supplemented with 0.1% polyvinyl alcohol to stabilize color development) was added to each quenched sample. After 2 minutes of incubation at room temperature, 2 µL of 34% (w/v) sodium citrate was added to chelate free molybdate and stabilize the color complex. Following a 30-minute incubation, the absorbance at 630 nm was measured using a CLARIOstar microplate reader (BMG Labtech). A standard curve was generated for each experiment using known concentrations of Na_2HPO_4 (0 to 600 µM) carried through the same detection protocol. The amount of Pi released (in nmol) was calculated from the standard curve. All assays were performed with three independent protein preparations.

Cryo-EM Sample Preparation, Data Collection, and Processing

Proteins for structural analysis were purified as described and concentrated to approximately 6 mg/mL. To identify optimal conditions for grid preparation, each sample was diluted to 1, 3, and 6 mg/mL before grid preparation. For cryo-EM grid preparation, 3 µL of the optimized protein sample was applied to freshly glow-discharged (15 mA, 30 s) holey carbon gold grids (Quantifoil Au R1.2/1.3, 300 mesh). Grids were blotted for 1.5 seconds under 95% humidity at 4°C using a Vitrobot Mark IV (Thermo Fisher Scientific) and plunge-frozen in liquid ethane. Grids from each concentration were screened, and the condition yielding the most homogeneous particle distribution and finest ice thickness was selected for high-resolution cryo-EM data collection.

Data were collected on a 300 kV Titan Krios G4 microscope (Thermo Fisher Scientific) equipped with a Cold-FEG electron source, a Gatan K3 Summit direct electron detector, and a Gatan Quantum LS energy filter (20 eV slit width). Micrographs were recorded in super-resolution counting mode using EPU (Thermo Fisher Scientific) at a nominal magnification of 105,000×, corresponding to a calibrated pixel size of 0.85 Å. A total exposure dose of 35 $e^{-}/Å^{2}$ was fractionated over 40 movie frames (2.5 s total exposure time), with a defocus range of − 1.0 to − 2.5 µm.

All data processing was performed in CryoSPARC v4.2.1. Movie frames were aligned using patch motion correction, and the contrast transfer function (CTF) was estimated with patch CTF estimation. Micrographs with poor CTF fits or significant ice contamination were removed during exposure curation. Particles were initially picked using a blob picker, extracted with a box size of 640 pixels, and subjected to multiple rounds of reference-free 2D classification. Selected particles were used for *ab initio* model generation and heterogeneous refinement. The final maps were obtained through homogeneous refinement with per-particle CTF refinement and Bayesian polishing. Detailed workflows for each dataset are provided in Supplementary Figs. 6 and 11, with data collection and refinement statistics summarized in Supplementary Table 1–3.

Model Building and Refinement

Initial atomic models of SopB (UniProt O30916) and SigE (UniProt O30917) were obtained from the AlphaFold2 database with the correspond ID: AF-O30916-F1 and AF-O30917-F1, respectively. These models were rigid-body docked into the cryo-EM density maps using UCSF Chimera and UCSF ChimeraX. Iterative cycles of manual adjustment for each residue were performed in Coot, and further overall real-space refinement were performed in Phenix to improve model geometry and fit. The final models were validated for stereochemistry and clash scores using MolProbity. Structural figures were prepared using UCSF ChimeraX and PyMOL. Refinement statistics dare summarized in Supplementary Table 1–3.

Molecular Dynamics Simulations

All-atom molecular dynamics (MD) simulations were performed to assess the conformational stability of SopB in its chaperone-bound and unbound states. The initial atomic coordinates were derived from our cryo-EM structures. Site-directed mutants (L76G/L79G, V526G/M527G, I555G/L558G) were modeled in PyMOL (Schrödinger LLC) by substituting the native side chains with glycine and sampling favorable rotamers. Simulations were conducted using the AMBER 20 software suite with the ff19SB force field.

Each system was solvated in a truncated octahedral box of TIP3P water molecules, extending at least 10 Å from the protein surface, and neutralized with NaCl to a concentration of 150 mM. To probe stability under denaturing conditions, parallel simulations were run at an elevated temperature (350 K). For each condition, three independent production runs of 500 ns each were performed, initiated with different random velocity seeds. Long-range electrostatics were treated with the Particle Mesh Ewald method, a 10 Å cutoff was applied to non-bonded interactions, and bonds involving hydrogen were constrained with the SHAKE algorithm, enabling a 2-fs integration timestep. For comparative validation of local unfolding dynamics, supplementary 50-ns simulations were performed using the SIMLab MD webserver (https://simlab.uams.edu), which utilizes GROMACS with the CHARMM36m force field under default solvation and parameter settings. Trajectory analysis, including root-mean-square deviation (RMSD) and root-mean-square fluctuation (RMSF), was conducted using the CPPTRAJ module in AMBER.

Cell Culture and Bacterial Infection

HeLa cells (ATCC CCL-2) were cultured in high-glucose Dulbecco's Modified Eagle Medium (DMEM; Gibco) supplemented with 10% (v/v) fetal bovine serum (FBS), 100 U/mL penicillin, and 100 µg/mL streptomycin at 37°C in a humidified 5% CO_2 atmosphere. For live-cell imaging, cells were seeded at 5 × 10^4 cells per well in 15-mm glass-bottom dishes 24 hours prior to infection. For immunofluorescence, cells were seeded at 6 × 10^4 cells per well on glass coverslips in 24-well plates. For infection, *Salmonella enterica serovar Typhimurium strains* (wild-type LT2 or isogenic Δsopb Δsope2 mutants) were grown statically overnight in LB at 37°C, subcultured 1:50 into fresh LB containing 80 µg/mL ampicillin and 0.15% L-arabinose (for pBAD induction), and grown with shaking (250 rpm) at 25°C to mid-log phase (OD_{600} 0.6–0.8). Bacteria were washed twice with PBS and resuspended in serum-free DMEM.

Cell monolayers were washed once with PBS before infection. Bacteria were added at a multiplicity of infection (MOI) of 100 for microscopy or MOI 50 for quantitative assays. Plates were centrifuged (1,000 × g, 5 min) to synchronize contact and incubated at 37°C for 1 hour.

Adhesion and Invasion Assays

Following the 1-hour infection, cells were washed three times with PBS to remove non-adherent bacteria. To quantify total cell-associated bacteria (adhesion), monolayers were immediately lysed with 0.5% Triton X-100 in PBS. To quantify intracellular bacteria (invasion), cells were incubated for an additional 1.5 hours in DMEM containing 50 µg/mL gentamicin before lysis. Lysates were serially diluted and plated on LB agar for colony-forming unit (CFU) enumeration. The inoculum was plated in parallel to determine the total bacterial count. Adhesion efficiency was calculated as (CFU recovered after washing / CFU in inoculum) × 100%. Invasion efficiency was calculated as (gentamicin-protected CFU / CFU in inoculum) × 100%.

Bacterial effector secretion assays

Bacterial cultures for secretion analysis were grown under the same conditions as for infection. For intracellular proteins, 1 mL of culture was pelleted (10,000 × g, 10 min, 4°C) and the bacterial pellet was

resuspended in 100 µL of 2.5× SDS-PAGE sample buffer. For secreted proteins, 10 mL of culture supernatant was filtered (0.22 µm) after centrifugation (15,000 × g, 20 min, 4°C). Proteins in the supernatant were precipitated overnight at 4°C with 10% (w/v) trichloroacetic acid, pelleted (20,000 × g, 40 min, 4°C), washed with ice-cold acetone, and resuspended in 2.5× SDS sample buffer. Samples were separated by SDS-PAGE, transferred to PVDF membranes, and immunoblotted using antibodies against HA-tag (1:5000, Proteintech 66006-2-Ig), His-tag (1:5000, Proteintech 66005-1-Ig), SopE2 (1:1000), and DnaK (1:10000, CUSABIO CSB-PA633459HA01EGW). For the detection of SopE2 protein, a custom-made rabbit polyclonal antibody was employed. This antibody was generated by immunizing rabbits with a recombinant expressed SopE2 protein (the C-terminal residues 69–240 of Salmonella SopE2). The antibody was produced and affinity-purified by Bioswamp Technology Co., Ltd., Wuhan, China.

Live-Cell pH Imaging and Secretion Directionality Assay

To measure local pH at the T3SS export apparatus, the pH probe, super-ecliptic pHluorin (SEP), was fused to the C-terminus of the major export apparatus protein InvA via a 10-amino-acid linker in a pBAD vector and expressed in the *S*. Typhimurium Δ*invA* strain. For cytosolic pH control, SEP was expressed alone from the same vector in the wild-type strain. A pH calibration standard curve was generated by measuring the 405 nm/488 nm excitation ratio ($R_{405}/_{488}$) of purified SEP in buffers of defined pH (4.9–8.0). The ratio was plotted against pH and fitted with a sigmoidal function in GraphPad Prism. The average pH of the local environment of bacteria was determined via the standard calibration curve using the $R_{405}/_{488}$ ratio.

For imaging, HeLa cells were infected with SEP-expressing strains (MOI 100, 1 h). In some experiments, the protonophore FCCP (20 µM final) was added at the time of infection. Cells were imaged on a Zeiss LSM 980 confocal microscope with a 63× oil objective, using sequential 405 nm and 488 nm excitation and collecting emission at 490–530 nm. The $R_{405}/_{488}$ for individual bacteria attached to cells was calculated using Fiji/ImageJ and converted to pH via the calibration curve.

To determine the direction of effector translocation, SEP was fused to either the N- or C-terminus of full-length SopB and expressed in the Δ*sopB* strain. The fluorescence color (488 nm, green for cytosolic, 405 nm, sky blue for acidic) of infected bacteria was quantified as described.

Immunofluorescence Microscopy

For immunofluorescence, HeLa cells on coverslips were infected with *S*. Typhimurium strains (MOI 100, 1 h). Bacteria were pre-labeled with 30 µM Cy3-NHS ester for 30 min at room temperature and washed before infection. After infection, cells were fixed with 4% paraformaldehyde, permeabilized with 0.2% Triton X-100, and blocked with 4% BSA. Cells were incubated overnight at 4°C with mouse anti-HA primary antibody (1:250), followed by Alexa Fluor 647-conjugated goat anti-mouse secondary antibody (1:250, Proteintech RGAM005) and Alexa Fluor 488-phalloidin (1:500, Abbkine BMD0082). Coverslips were mounted with ProLong Gold Antifade containing DAPI (Abbkine BMU107). Images were acquired on a Zeiss LSM 980 confocal microscope and analyzed with Fiji/ImageJ.

Statistics and Reproducibility

Statistical analyses were performed using GraphPad Prism 11.0. Data are presented as the mean ± standard error of the mean (SEM) from at least three independent biological replicates. The specific statistical test applied to each dataset is indicated in the corresponding figure legend. For comparisons among multiple groups, one-way analysis of variance (ANOVA) was performed, followed by Dunnett's post-hoc test when comparing all conditions to a single control group. A p-value of less than 0.05 was considered statistically significant (*p* < 0.05; **p* < 0.01; ***p* < 0.001; ****p* < 0.0001). No statistical methods were used to predetermine sample size, and no data were excluded from the analyses. Experiments were not randomized, and investigators were not blinded to allocation during experiments and outcome assessment, except where specified.

Declarations

Data availability

The cryo-EM density maps for the SopB, and the SigE-SopB complex at various pH conditions as well as the SopB mutants have been deposited in the Electron Microscopy Data Bank under accession codes EMD-36746, EMD-67333, EMD-67332, EMD-67342, EMD-67334, EMD-67350 and EMD-67351. The corresponding atomic coordinates have been deposited in the Protein Data Bank under accession codes 8JZL, 9XWE, 9XWB, 9XWS, 9XWF, 9XX6, and 9XX7. Source data for all graphs and charts presented in the main figures are provided as a Source Data file. Raw gel and blot images are available in Supplementary Information. All other data supporting the findings of this study are available within the article and its Supplementary Information files.

Acknowledgments and Funding

We thank the staff of the Cryo-EM Center and the Computational Center of Hubei University for technical support, with special thanks to Dr. Qianjun Chen and Dr. Hong Yang for assistance with data collection and processing. NMR experiments were performed at the National Center for Magnetic Resonance in Wuhan. This work was supported by the National Natural Science Foundation of China (grants 32371277 to Q.X. and 32301028 to W.J.), the Project of Technological Innovation Plan in Hubei Province (2024BCA001 to Q.X.), and the Hubei Province Science and Technology Plan Project (2021CSA066 to Q.X.).

Contributions

Q.X. conceptualized the project and designed the experiments. W.X.J., and M.W performed the majority of experiments including gene cloning, protein purification, biochemical and cellular assays, and data analysis. X.Q.C. prepared cryo-EM samples, performed grid screening, and data collection. Q.X. and W.X.J carried out the cryo-EM data process, model building and refinement. D.J.S assisted with protein sample preparation. Z.G performed and analyzed MD simulations. Q.X., W.X.J., and M.W. wrote the

paper. X.D. and L.X.M. provided critical feedback and contributed to the discussion of the results. All authors reviewed, edited, and approved the final manuscript.

Lead Contact and Resource Availability

Further information and requests for resources and reagents could be directed to and will be fulfilled by the lead contact: Dr Qiong Xing, qiongxingnmr@hubu.edu.cn

Declaration of interests

The authors declare no competing interests.

References

1. Galan, J. E. & Wolf-Watz, H. Protein delivery into eukaryotic cells by type III secretion machines. *Nature* **444**, 567-573, doi:10.1038/nature05272 (2006).
2. Costa, T. R. *et al.* Secretion systems in Gram-negative bacteria: structural and mechanistic insights. *Nat Rev Microbiol* **13**, 343-359, doi:10.1038/nrmicro3456 (2015).
3. Coburn, B., Sekirov, I. & Finlay, B. B. Type III secretion systems and disease. *Clin Microbiol Rev* **20**, 535-549, doi:10.1128/CMR.00013-07 (2007).
4. Deng, W. *et al.* Assembly, structure, function and regulation of type III secretion systems. *Nat Rev Microbiol* **15**, 323-337, doi:10.1038/nrmicro.2017.20 (2017).
5. Remick, B. C., Gaidt, M. M. & Vance, R. E. Effector-Triggered Immunity. *Annu Rev Immunol* **41**, 453-481, doi:10.1146/annurev-immunol-101721-031732 (2023).
6. Worrall, L. J., Majewski, D. D. & Strynadka, N. C. J. Structural Insights into Type III Secretion Systems of the Bacterial Flagellum and Injectisome. *Annu Rev Microbiol* **77**, 669-698, doi:10.1146/annurev-micro-032521-025503 (2023).
7. Bergeron, J. R. C. & Marlovits, T. C. Cryo-EM of the injectisome and type III secretion systems. *Curr Opin Struct Biol* **75**, 102403, doi:10.1016/j.sbi.2022.102403 (2022).
8. Zierler, M. K. & Galan, J. E. Contact with cultured epithelial cells stimulates secretion of Salmonella typhimurium invasion protein InvJ. *Infect Immun* **63**, 4024-4028, doi:10.1128/iai.63.10.4024-4028.1995 (1995).
9. Menard, R., Sansonetti, P. & Parsot, C. The secretion of the Shigella flexneri Ipa invasins is activated by epithelial cells and controlled by IpaB and IpaD. *EMBO J* **13**, 5293-5302, doi:10.1002/j.1460-2075.1994.tb06863.x (1994).
10. Ruano-Gallego, D. *et al.* Type III secretion system effectors form robust and flexible intracellular virulence networks. *Science* **371**, doi:10.1126/science.abc9531 (2021).
11. Miletic, S. *et al.* Substrate-engaged type III secretion system structures reveal gating mechanism for unfolded protein translocation. *Nat Commun* **12**, 1546, doi:10.1038/s41467-021-21143-1 (2021).

12. LeBlanc, M. A., Fink, M. R., Perkins, T. T. & Sousa, M. C. Type III secretion system effector proteins are mechanically labile. *Proc Natl Acad Sci U S A* **118**, doi:10.1073/pnas.2019566118 (2021).
13. Green, E. R. & Mecsas, J. Bacterial Secretion Systems: An Overview. *Microbiol Spectr* **4**, doi:10.1128/microbiolspec.VMBF-0012-2015 (2016).
14. Yu, X. J., McGourty, K., Liu, M., Unsworth, K. E. & Holden, D. W. pH sensing by intracellular Salmonella induces effector translocation. *Science* **328**, 1040-1043, doi:10.1126/science.1189000 (2010).
15. Lara-Tejero, M. & Galan, J. E. The Injectisome, a Complex Nanomachine for Protein Injection into Mammalian Cells. *EcoSal Plus* **8**, doi:10.1128/ecosalplus.ESP-0039-2018 (2019).
16. Galan, J. E. & Waksman, G. Protein-Injection Machines in Bacteria. *Cell* **172**, 1306-1318, doi:10.1016/j.cell.2018.01.034 (2018).
17. Akeda, Y. & Galan, J. E. Chaperone release and unfolding of substrates in type III secretion. *Nature* **437**, 911-915, doi:10.1038/nature03992 (2005).
18. Erhardt, M., Mertens, M. E., Fabiani, F. D. & Hughes, K. T. ATPase-independent type-III protein secretion in Salmonella enterica. *PLoS Genet* **10**, e1004800, doi:10.1371/journal.pgen.1004800 (2014).
19. Lee, P. C. & Rietsch, A. Fueling type III secretion. *Trends Microbiol* **23**, 296-300, doi:10.1016/j.tim.2015.01.012 (2015).
20. Minamino, T. & Namba, K. Distinct roles of the FliI ATPase and proton motive force in bacterial flagellar protein export. *Nature* **451**, 485-488, doi:10.1038/nature06449 (2008).
21. Minamino, T., Morimoto, Y. V., Hara, N., Aldridge, P. D. & Namba, K. The Bacterial Flagellar Type III Export Gate Complex Is a Dual Fuel Engine That Can Use Both H+ and Na+ for Flagellar Protein Export. *PLoS Pathog* **12**, e1005495, doi:10.1371/journal.ppat.1005495 (2016).
22. Schlumberger, M. C. *et al.* Real-time imaging of type III secretion: Salmonella SipA injection into host cells. *Proc Natl Acad Sci U S A* **102**, 12548-12553, doi:10.1073/pnas.0503407102 (2005).
23. Fritsch, V. N. & Hensel, M. Experimental Approaches to Visualize Effector Protein Translocation During Host-Pathogen Interactions. *Bioessays* **47**, e202400188, doi:10.1002/bies.202400188 (2025).
24. Van Engelenburg, S. B. & Palmer, A. E. Quantification of real-time Salmonella effector type III secretion kinetics reveals differential secretion rates for SopE2 and SptP. *Chem Biol* **15**, 619-628, doi:10.1016/j.chembiol.2008.04.014 (2008).
25. Galan, J. E. Common themes in the design and function of bacterial effectors. *Cell Host Microbe* **5**, 571-579, doi:10.1016/j.chom.2009.04.008 (2009).
26. Arnold, R. *et al.* Sequence-based prediction of type III secreted proteins. *PLoS Pathog* **5**, e1000376, doi:10.1371/journal.ppat.1000376 (2009).
27. Stebbins, C. E. & Galan, J. E. Maintenance of an unfolded polypeptide by a cognate chaperone in bacterial type III secretion. *Nature* **414**, 77-81, doi:10.1038/35102073 (2001).

28. Xing, Q. *et al.* Structures of chaperone-substrate complexes docked onto the export gate in a type III secretion system. *Nat Commun* **9**, 1773, doi:10.1038/s41467-018-04137-4 (2018).
29. Lilic, M., Vujanac, M. & Stebbins, C. E. A common structural motif in the binding of virulence factors to bacterial secretion chaperones. *Mol Cell* **21**, 653-664, doi:10.1016/j.molcel.2006.01.026 (2006).
30. Radics, J., Konigsmaier, L. & Marlovits, T. C. Structure of a pathogenic type 3 secretion system in action. *Nat Struct Mol Biol* **21**, 82-87, doi:10.1038/nsmb.2722 (2014).
31. Gilzer, D., Schreiner, M. & Niemann, H. H. Direct interaction of a chaperone-bound type III secretion substrate with the export gate. *Nat Commun* **13**, 2858, doi:10.1038/s41467-022-30487-1 (2022).
32. Sorg, J. A., Miller, N. C., Marketon, M. M. & Schneewind, O. Rejection of impassable substrates by Yersinia type III secretion machines. *J Bacteriol* **187**, 7090-7102, doi:10.1128/JB.187.20.7090-7102.2005 (2005).
33. Dohlich, K., Zumsteg, A. B., Goosmann, C. & Kolbe, M. A substrate-fusion protein is trapped inside the Type III Secretion System channel in Shigella flexneri. *PLoS Pathog* **10**, e1003881, doi:10.1371/journal.ppat.1003881 (2014).
34. Ghosh, P. Process of protein transport by the type III secretion system. *Microbiol Mol Biol Rev* **68**, 771-795, doi:10.1128/MMBR.68.4.771-795.2004 (2004).
35. Ernst, N. H., Reeves, A. Z., Ramseyer, J. E. & Lesser, C. F. High-Throughput Screening of Type III Secretion Determinants Reveals a Major Chaperone-Independent Pathway. *mBio* **9**, doi:10.1128/mBio.01050-18 (2018).
36. Miesenböck, G., De Angelis, D. A. & Rothman, J. E. Visualizing secretion and synaptic transmission with pH-sensitive green fluorescent proteins. *Nature* **394**, 192-195, doi:10.1038/28190 (1998).
37. Giska, F. *et al.* Noncanonical calcium binding motif controls folding of HopQ1, a Pseudomonas syringae type III secretion effector, in a pH-dependent manner. *Sci Rep* **14**, 31796, doi:10.1038/s41598-024-82848-z (2024).
38. Dawson, J. E. *et al.* Elucidation of a pH-folding switch in the Pseudomonas syringae effector protein AvrPto. *Proc Natl Acad Sci U S A* **106**, 8543-8548, doi:10.1073/pnas.0809138106 (2009).
39. Gooran, N. & Kopra, K. Fluorescence-Based Protein Stability Monitoring-A Review. *Int J Mol Sci* **25**, doi:10.3390/ijms25031764 (2024).
40. Martins de Oliveira, V. *et al.* Effects of pH and Salt Concentration on Stability of a Protein G Variant Using Coarse-Grained Models. *Biophys J***114**, 65-75, doi:10.1016/j.bpj.2017.11.012 (2018)

Figures

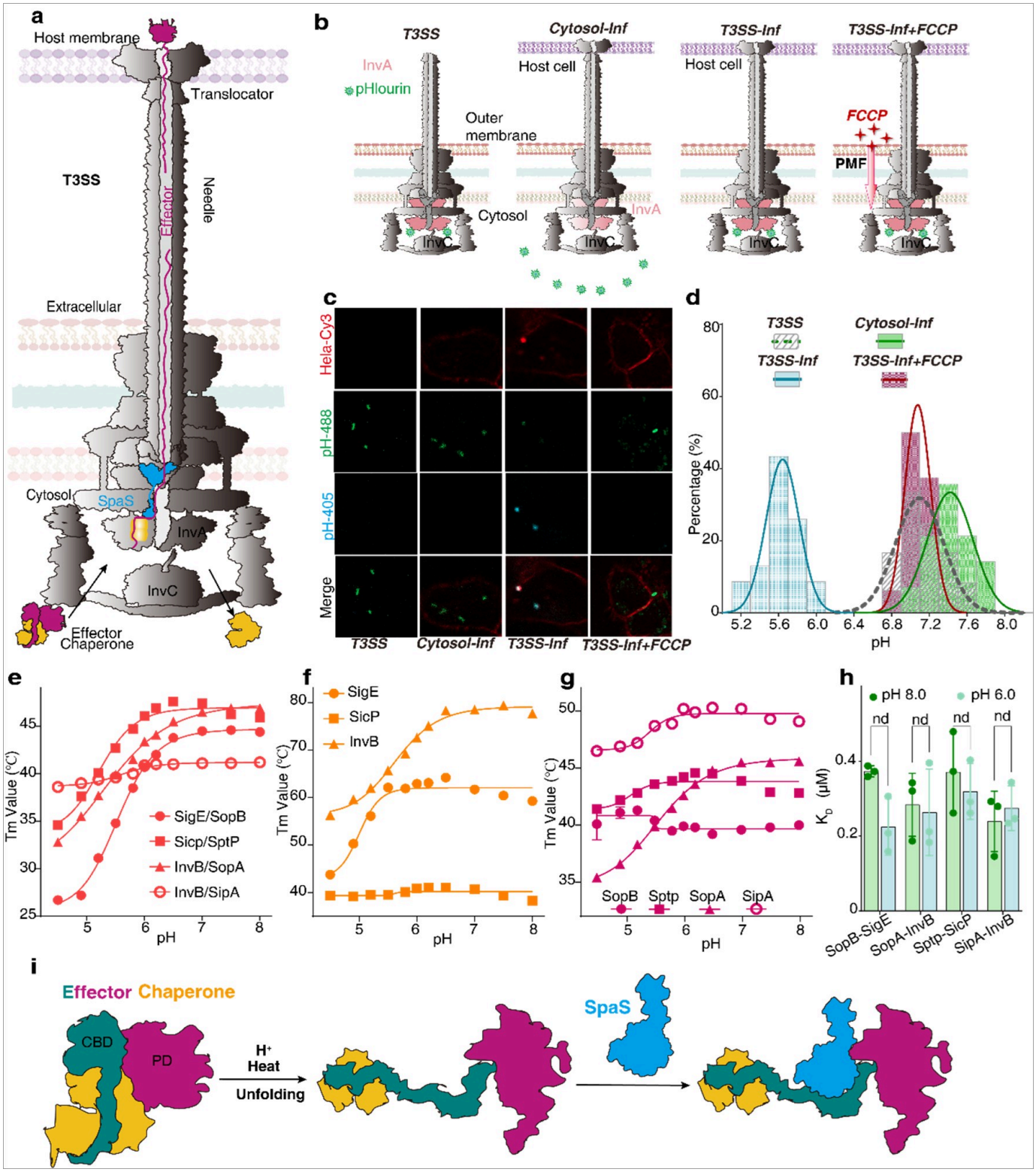

Figure 1

Host cell contact generates an acidic microenvironment at the T3SS export apparatus to license effector unfolding and targeting.

a, Schematic of the *Salmonella* Type III Secretion System (T3SS) injectisome at the host–pathogen interface during effector secretion. Core apparatus components are shown in grey; the cytosolic

gatekeeper SpaS is shown in sky blue. An effector (dark magenta) is bound by its cognate chaperone (yellow) prior to engagement with the secretion machinery.

b, Strategy for measuring local pH at the cytosolic face of the T3SS export apparatus. The ratiometric pH-sensitive fluorophore super-ecliptic pHluorin (SEP, dark green) was fused to the C terminus of the export apparatus protein InvA (red) and expressed in a ΔinvA background. Four experimental conditions were analyzed: T3SS, InvA–SEP bacteria in culture (no host contact); Cytosol-inf, bacteria expressing cytosolic SEP during host cell infection; T3SS-inf, InvA–SEP bacteria during host cell infection; and T3SS-inf + FCCP, InvA–SEP bacteria during infection in the presence of the protonophore FCCP (20 μM).
c, Representative confocal micrographs of S. Typhimurium attached to HeLa cells under the four conditions. Host cells are labeled with CellTracker™ Red CMTPX (red). SEP fluorescence was collected upon excitation at 405 nm (cyan) and 488 nm (green). The 405/488 nm emission ratio reports local pH (see Methods).
d, Quantification of local pH at the T3SS export apparatus. pH values from individual bacteria (n > 15 per condition) were pooled and fitted to Gaussian distributions. Mean pH ± s.d.: T3SS, 7.10 ± 0.25; Cytosol-inf, 7.42 ± 0.24; T3SS-inf, 5.64 ± 0.17; T3SS-inf + FCCP, 7.08 ± 0.14.
e-g, pH-dependent thermal stability of chaperone–effector complexes measured by differential scanning fluorimetry (SYPRO Orange). Data represent mean melting temperature (Tm) ± s.d. from three independent experiments.
e, Tm of three canonical chaperone-effector complexes (SigE-SopB, SicP-SptP, InvB-SopA, InvB-SipA) across a pH gradient.
f, Tm values of chaperones alone (SigE, SicP, InvB).
g, Tm of effectors alone (SopB, SptP, SopA, SipA).
h, Isothermal titration calorimetry (ITC) analysis of chaperone–effector binding affinities at pH 6.0 and pH 8.0. Representative binding isotherms are shown; mean dissociation constants (K_D) were derived from three independent experiments (n.d., not defined).
i, Model for pH- and temperature-dependent recognition of chaperone-bound effectors by the gatekeeper SpaS, informed by solution-state NMR titration. At neutral pH and low temperature, the chaperone-binding domain (teal) and functional domain (magenta) of the effector remain folded and inaccessible to SpaS. Under acidic pH or destabilizing thermal conditions, the effector undergoes partial unfolding while remaining chaperone-bound, exposing polypeptide segments that are selectively recognized by SpaS to initiate secretion.

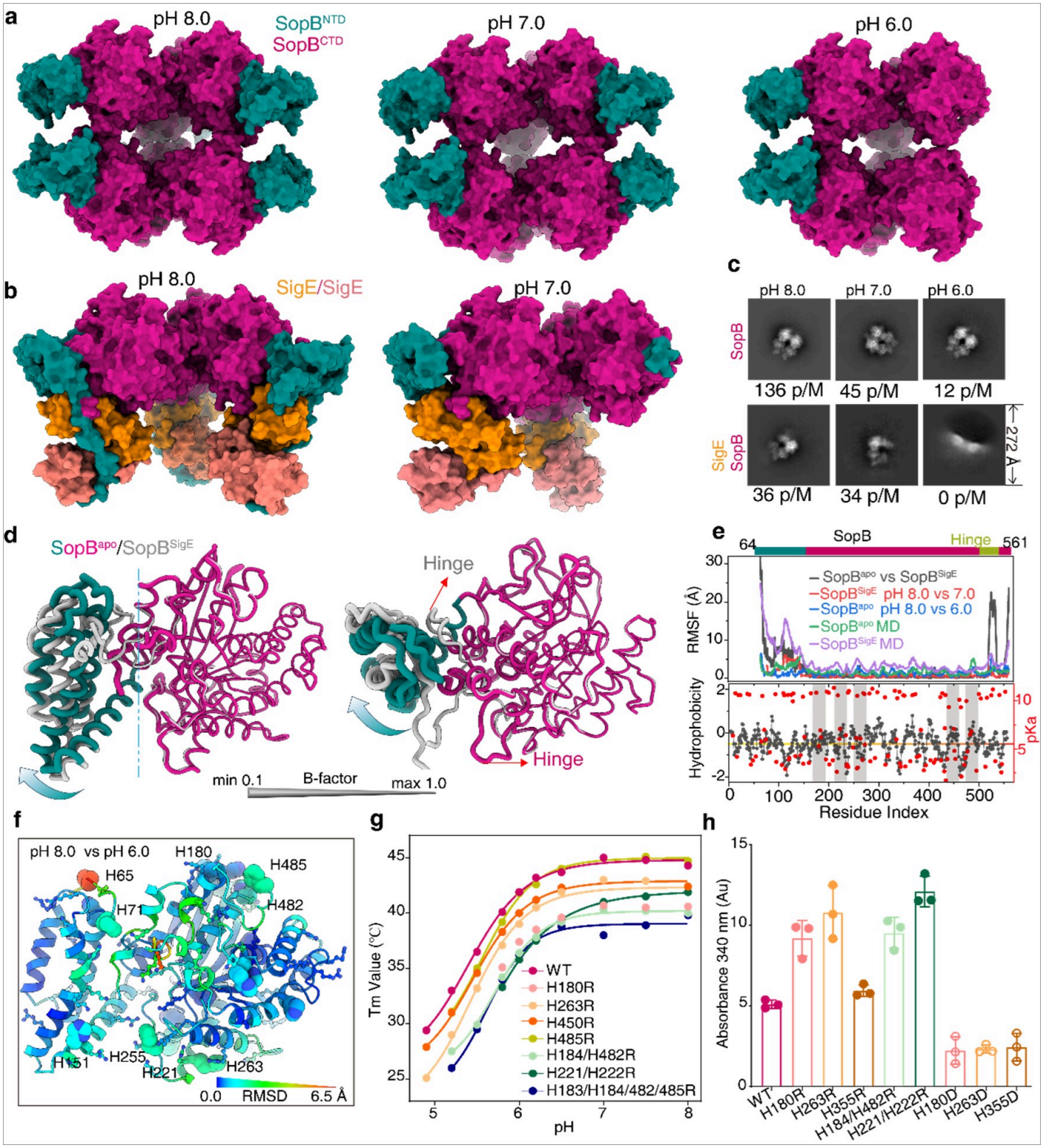

Figure 2

Structural and biochemical characterization of effector alone and chaperone-effector complex at various pH.

a, Surface representations of the cryo-EM structure of the SopB hexamer at pH 8.0, 7.0, and 6.0. The chaperone-binding domain (teal) and the C-terminal functional domain (magenta) are indicated.

b, Surface representations of the SigE-SopB complex (trimer of heterodimers) at pH 8.0 and 7.0. The SigE chaperone homodimer is shown in yellow and orange.
c, Representative reference-free 2D class averages from cryo-EM datasets of SopB alone and the SigE–SopB complex at the indicated pH values with average particle numbers used for structure determination indicated.
d, Structural superposition of SopB in its free (grey) and SigE-bound (teal and magenta) states, shown as a cylinder representation scaled to local B-factor (thickness indicates flexibility). A major destabilized hinge region at the NTD-CTD interface is highlighted (arrow).
e, Per-residue root-mean-square fluctuation (RMSF) analysis comparing conformational dynamics under different conditions. Experimental cryo-EM-derived flexibility profiles are shown for SopB_apo at pH 8.0 (grey) and pH 6.0 (light blue), and for SigE–SopB at pH 8.0 and 7.0 (red). RMSF profiles from 500-ns molecular dynamics simulations are overlaid for SopB_apo (green) and SigE–SopB (purple). Below, the Roseman hydrophobicity profile (window = 9) and predicted residue *pKa* values (DeepKa) are shown, highlighting potential pH-sensitive regions.
f, Structural changes within a SopB monomer upon acidification, visualized by Cα RMSD mapping between pH 8.0 and pH 6.0 structures (blue, 0 Å; red, >6.5 Å). Histidine side chains are shown as spheres, and surrounding basic residues (Arg/Lys) are shown as sticks, illustrating pH-sensitive electrostatic networks.
g, Thermal stability of SigE–SopB complexes containing histidine-to-arginine substitutions. Differential scanning fluorimetry reveals pronounced pH-dependent destabilization upon H→R mutation, with additive effects observed in multi-site mutants (e.g., H183/184/482/485R), consistent with constitutive protonation of the pH-sensing network.
h, Aggregation propensity of SopB histidine mutants at pH 5.5, measured by light scattering (A_{340}). H→R mutants increase aggregation, whereas histidine-to-aspartate substitutions (H→D) suppress aggregation, confirming the role of histidine protonation in destabilizing the primed effector. Data are mean ±s.d. (n = 3).

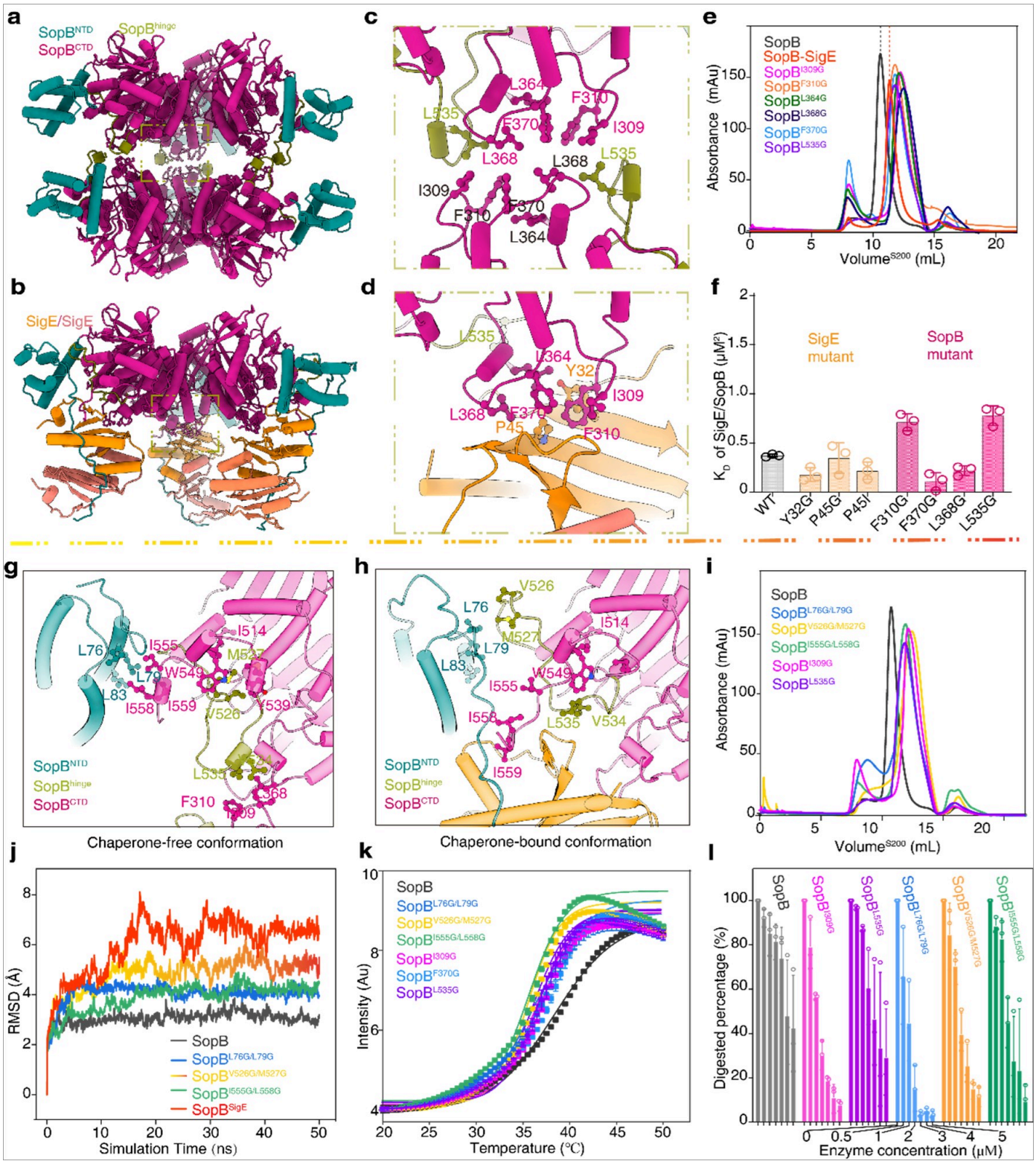

Figure 3

Chaperone binding disrupts oligomeric and interdomain interfaces to prime SopB for unfolding.

a, Cartoon representation of the SopB homohexamer. The N-terminal chaperone-binding domain (CBD, teal), the C-terminal functional (phosphatase) domain (PD, magenta), and the interdomain hinge (olive) are indicated.

b, Structure of the SigE-SopB complex. Chaperone binding disassembles the SopB hexamer into a trimer of 1:1 heterodimers, with each SopB monomer bound by a SigE homodimer (yellow/orange).
c,d, Close-up views of key interfaces. **(c)** Residues mediating the trimer-trimer interface in the SopB hexamer. **(d)** Residues at the SigE-SopB binding interface.
e, Analytical size-exclusion chromatography profiles of wild-type SopB (grey), the SigE-SopB complex (red), and SopB mutants designed to disrupt hexameric packing (I309G, F310G, L364G, L368G, F370G, L535G).
f, Binding affinities (K_D) determined by ITC for SigE binding to wild-type SopB or interface mutants. Data are mean ± s.d. (n=3). Mutations at the SigE-SopB interface (Y32G, P45G, P45I in SigE; F310G, F370G in SopB) did not significantly weak binding, while mutations at the hexameric interface (L364G, L535G in SopB) have minimal effect.
g,h, Close-up of the intradomain CBD-PD interface in **(g)** SopB_apo and **(h)** the SigE-bound state, showing key interacting residues.
i, Analytical SEC profiles of SopB mutants designed to disrupt the intradomain CBD-PD interface (L76G/L79G, V526G/M527G, I555G/L558G).
j, Per-residue RMSF from MD simulations comparing wild-type SopB apo (grey), SigE-bound SopB (red), and intradomain interface mutants (L76G/L79G, V526G/M527G, I555G/L558G). Mutants exhibit elevated flexibility mimicking the chaperone-bound state.
k,l, Functional consequences of interface disruption. **(k)** Thermal stability (Tm at pH 7.5) of wild-type SopB and mutants. **(l)** Protease susceptibility (fraction cleaved by subtilisin) of the same proteins. Disruption of either the hexameric (I309G, F370G, L535G) or interdomain (L76/79G, V526/527G, I555/558G) interface destabilizes SopB. Data are presented as mean ± s.d. (n=3).

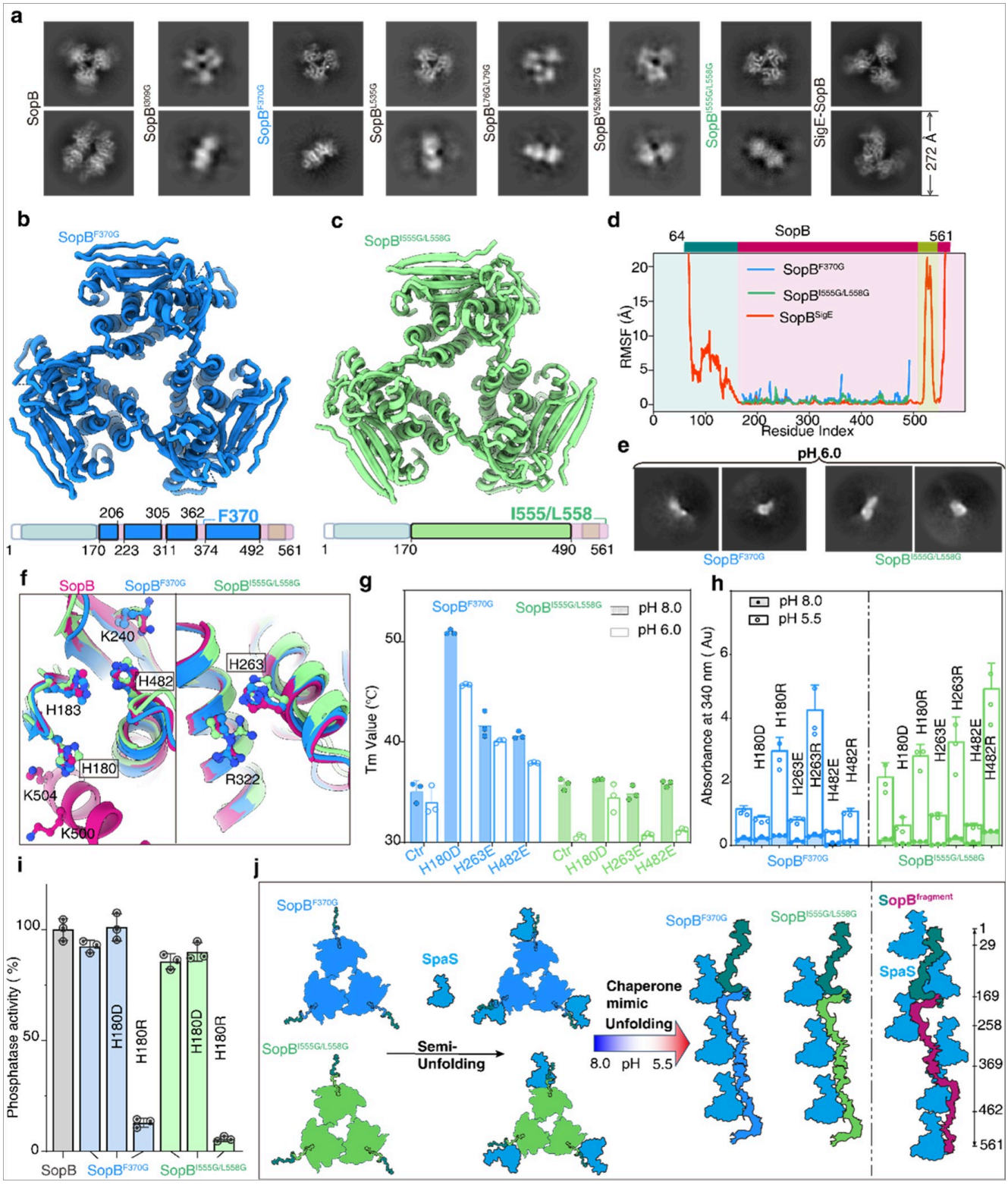

Figure 4

Mutants disrupting oligomeric or intradomain interfaces constitutively adopt a chaperone-primed, pH-sensitive state.

a, Representative reference-free 2D class averages from cryo-EM datasets of wild-type SopB, the SigE–SopB complex, and SopB variants disrupting either the hexameric interface (I309G, F370G, L535G) or the

intradomain CBD–PD interface (L76G/L79G, V526G/M527G, I555G/L558G). Interface mutants exhibit increased structural heterogeneity resembling the chaperone-bound state. Box size, 272 Å.
b,c, Cryo-EM structures of chaperone-free SopB mutants. **(b)** F370G mutant (sky blue) disrupting the hexameric interface. **(c)** I555G/L558G mutant (light green) disrupting the intradomain interface. Bar representations underneath the structures are shown with a schematic indicating visible regions of the polypeptide chain (solid box) and disordered regions (transparent box). Mutation sites are indicated.
d, Per-residue RMSF analysis comparing different states with wild-type SopB, including the SigE-bound state (grey), and the F370G (sky blue) and I555G/L558G (light green) mutants. Both mutants display elevated flexibility, particularly within the N-terminal domain and interdomain hinge, phenocopying the chaperone-primed conformation.
e, Reference-free 2D class averages of F370G and I555G/L558G mutants at pH 6.0, revealing enhanced conformational heterogeneity consistent with further acid-induced unfolding.
f, Structural overlay of wild-type SopB (magenta) and interface mutants highlighting conserved histidine residues (H180, H263, H482) implicated in pH sensing. Histidines are labeled; surrounding basic residues (Arg, Lys) are shown as sticks, illustrating electrostatic environments susceptible to protonation-induced destabilization
g, Thermal stability of interface mutants and their histidine variants. Tm values for the F370G and I555G/L558G mutants (controls) and derivatives where key histidine is mutated to aspartate/glutamate (H→D/E) are shown at pH 8.0 (solid bars) and 6.0 (open bars). H→D/E mutations in the context of disrupted pH sensors function to restore stability at low pH.Data are presented with bar chart and shown mean values ± s.d. (n=3).
h, Aggregation propensity (A_{340}) of the same mutant series at pH 5.5 and 8.0. Mimicking histidine protonation (H→R) increases aggregation at low pH in interface mutants, while introducing negative charge (H→D/E) suppresses it. Data are mean ± s.d. (n=3).

j, Model for SpaS-mediated recognition, positioning, and processive engagement of unfolded effector substrates. NMR titration experiments show that the cytosolic domain of SpaS interacts with chaperone-mimetic SopB mutants (F370G and I555G/L558G) at neutral pH (7.5), with binding markedly enhanced at acidic pH (6.0). NMR analysis using SopB fragments spanning the full-length sequence reveals that SpaS recognizes multiple independent, unstructured segments. These findings support a model in which SpaS selectively engages primed, unfolded effectors and acts as a multivalent, processive anchor that sequentially captures emerging polypeptide segments, thereby orienting and feeding the substrate into the T3SS channel for translocation.

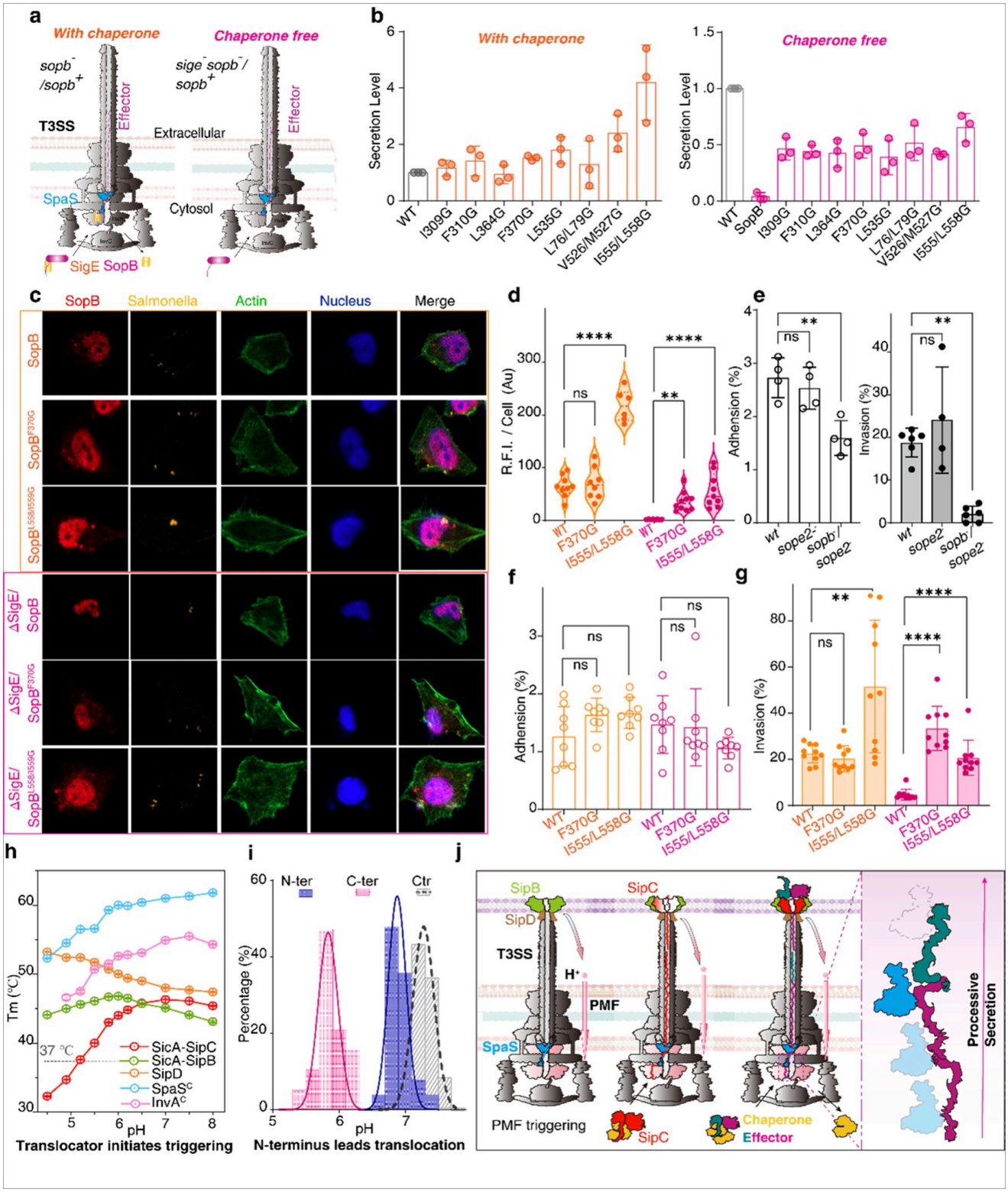

Figure 5

Constitutively primed effector mutants bypass the chaperone requirement for secretion, translocation, and host cell invasion.

a, Schematic of experimental systems used to assess SopB secretion and function. With chaperone: a *ΔsopB* strain complemented with plasmids expressing wild-type or mutant SopB in the presence of the

cognate chaperone SigE. Chaperone-free: a *ΔsopBΔsigE* strain expressing SopB variants from plasmids in the absence of SigE.
b, Secretion of HA-tagged SopB variants into culture supernatants. Immunoblots show secretion efficiency in the presence (left) or absence (right) of SigE for wild-type SopB and interface-disrupting mutants. Constitutively primed mutants are efficiently secreted without the chaperone. Blots are representative of three independent experiments.
c, Immunofluorescence microscopy of infected HeLa cells. Cells were infected with *S. Typhimurium* Δ*sopB* (with chaperone, only *sopB* knockout, orange outline) or Δ*sopB*Δ*sigE* (chaperone-free, magenta outline) strains expressing HA-tagged SopB variants. Bacteria (yellow, Cy3), SopB (red, anti-HA), actin (green, phalloidin), and nuclei (blue, DAPI).
d, Quantification of intracellular SopB fluorescence intensity from (c) (n ≥ 8 cells per condition). Data were analyzed by one-way ANOVA with Tukey's post hoc test ($p < 0.05$; *$p < 0.01$; **$p < 0.001$; ***$p < 0.0001$).
e, Adhesion and invasion efficiencies of wild-type, ΔsopB, and ΔsopBΔsopE2 *S. Typhimurium* strains. Data are mean ± s.d. (n = 3).
f,g, Adhesion (**f**) and invasion (**g**) efficiencies of ΔsopBΔsopE2 strains complemented with plasmids expressing wild-type SopB or constitutively primed mutants (F370G, I555G/L558G). Primed mutants restore invasion independently of SigE. Data are mean ± s.d. (n = 3).
h, Thermal stability of additional T3SS substrate–chaperone complexes, substrates, and regulatory components across a pH gradient, including the translocator complexes SicA–SipC and SicA–SipB, the needle tip protein SipD, and the cytosolic domains of InvA and SpaS. Among all substrates tested, only SipC in complex with its chaperone SicA exhibits pronounced pH-dependent destabilization, consistent with a shared priming logic during early translocon assembly.
i, Directionality of effector engagement assessed using N- or C-terminal pHluorin fusions to SopB. Local pH at the export apparatus was measured in bacteria expressing pHluorin–SopB (N-terminal fusion) or SopB–pHluorin (C-terminal fusion). Acidification is selectively detected when the N terminus is proximal to the export gate, consistent with N-terminal engagement during translocation. Data represent Gaussian-fitted distributions from >15 bacteria per condition. Mean pH ± s.d.: no-host control, 7.28 ± 0.16; pHluorin–SopB, 5.83 ± 0.15; SopB–pHluorin, 6.88 ± 0.13.
j, Integrated model of the "prime-and-trigger" secretion mechanism. (1) Prior to host contact, the local pH at the T3SS export apparatus is neutral. (2) Host-cell attachment and translocator (SipB) insertion initiates PMF-dependent proton accumulation, generating a localized acidic niche. (3) This acidic signal selectively destabilizes chaperone-primed effectors, inducing partial unfolding. (4) The unfolded effector is engaged segment-by-segment by SpaS and processively translocated through the secretion channel.

Supplementary Files

This is a list of supplementary files associated with this preprint. Click to download.

- updateNMreportingsummary0430.pdf

- GraphicAbstract.png
- Structuralvalidationreports.rar